Tuning the microwave electromagnetic properties of biochar-based composites by annealing

Carbon Trends 4 (2021) 100062

Contents lists available at ScienceDirect

Carbon Trends

journal homepage: www.elsevier.com/locate/cartre

Tuning the microwave electromagnetic properties of biochar-based composites by annealing

Daniele Torsello[a,b], Gianluca Ghigo[a,b,*], Mauro Giorcelli[c,d], Mattia Bartoli[a,c], Massimo Rovere[a,c], Alberto Tagliaferro[a,c,e,*]

[a] Department of Applied Science and Technology, Politecnico di Torino, C.so Duca degli Abruzzi 24, 10129 Turin, Italy
[b] Istituto Nazionale di Fisica Nucleare, Sez. Torino, Via P. Giuria 1, 10125 Torino, Italy
[c] Consorzio Interuniversitario Nazionale per la Scienza e Tecnologia dei Materiali (INSTM), Via G. Giusti 9, 50121 Florence, Italy
[d] Italian Institute of Technology, Via Livorno 60, 10144 Torino, Italy
[e] Faculty of Science, Ontario Tech University, 2000 Simcoe Street North, Oshawa, Ontario, Canada

ARTICLE INFO

Article history:
Received 8 March 2021
Revised 12 April 2021
Accepted 5 May 2021

Keywords:
Biochar composites
Raman analysis
XPS analysis
Biochar annealing
Microwave characterization
Complex permittivity

ABSTRACT

We report on the effects of thermal treatment of biochar embedded in epoxy-based composites on their microwave electrical properties, linking such properties to the material structure investigated by Raman, X-ray photoelectron spectroscopy, and X-ray diffraction. Annealing temperatures in the range 900–1500 °C and biochar concentrations in the epoxy matrix in the range from 5 to 25 wt.% were investigated. The microwave analysis, in the range from 250 MHz to 6 GHz, allowed us to determine the complex permittivity of composites and, through a proper deconvolution technique, to determine the contribution of biochar inclusions alone. High values of real permittivity (up to 220) and conductivity (up to 17 S/m) were evaluated for the biochar particles at 5 GHz, after the 1500 °C thermal treatment. A clear correlation between electrical properties and the biochar microstructure emerged from the dataset, with real permittivity and conductivity increasing as carbon inclusions transform from amorphous to nanocrystalline graphite. Conversely, the percentage of aromatic carbon has a weaker influence on the microwave properties. This study opens to the possibility of tailoring the high-frequency properties of biochar and biochar composites through proper thermal treatments.

1. Introduction

Nowadays, the worldwide attention is focused on environmental threats, and innovations aimed at preserving the earth resources are finally a primary goal. This new state of mind represents an astonishing driving force for the development of sustainable processes and materials [1]. In this regard, a special attention has been focused on carbon-based materials that are very well-established commodities [2] used for many applications [3,4]. Among the various sustainable carbon materials, biochar is highly promising, due to its low cost (of around 0.8–2.4 €/kg [5]), and its performance and tuneable properties [6]. These features, together with a reduced environmental footprint, promise a new era for materials science [7].

Actually, the most widespread uses of biochar are as soil amendment [8] or as solid fuel, but it has a great potential for plenty of other applications [7]. Among them, the production of biochar-based composites is of high interest due to the growing demand of several industrial sectors for affordable and high performances carbon-based composites. In this framework, Khan et al. [9,10] used biochar as efficient replacement for carbon nanotubes (CNT) reaching better mechanical performances. Moreover, several studies clearly showed that biochar could enhance selectively both brittleness or ductility based on feedstocks [11], temperature [12] and particle shape [13].

Mechanical enhancement is neither the only improvement induced by biochar nor the most interesting. Biochar-based composites remarkably showed properties comparable with those achieved by using expensive nanostructured fillers such as graphene and CNT.

Nonetheless, biochar optimization seems to require high temperature treatments to improve the dimension and quality of the

* Corresponding authors.
E-mail addresses: gianluca.ghigo@polito.it (G. Ghigo), alberto.tagliaferro@polito.it (A. Tagliaferro).

https://doi.org/10.1016/j.cartre.2021.100062

Table 1
Samples labelling.

Samples labelling	Treatment temperature [°C]
OSR 550	550[a]
OSR 900	900[b]
OSR 1100	1100[b]
OSR 1500	1500[b]

[a] Pyrolysis process.
[b] annealing process.

graphitic domains [14,15]. Although the graphitization of biochar, even if improved by using pyrolysis temperature over 800°C [12,16–18], remains far from those of neat CNT and graphene, its higher dispersibility allows reaching similar overall properties in the composites.

Accordingly, post-production thermal annealing has been shown to be a very effective way to increase the electrical conductivity of biochar [19–21]. A strong conductivity enhancement was observed for annealing temperature of up to 1000 °C due to the formation and reorganization through turbostratic rearrangement [22] of graphitic domains [23].

In this work, we evaluate in detail the relation between the thermal treatment of biochar and its electrical properties by correlating microwave measurements with structural features deduced by Raman, X-ray photoelectron spectroscopy (XPS) and X-ray diffraction (XRD) analysis. Furthermore, we analyze the effect of highly conductive biochar on permittivity and conductivity of epoxy-based composites in a wide range of concentrations. The use of a microwave characterization technique allowed us to address the topic – relevant for applications – of the high-frequency response of biochar, when embedded in a composite material. The aim of this study is in fact to explore the possibility of tailoring the high-frequency properties of biochar and biochar composites through proper thermal treatments.

2. Materials and methods

2.1. Materials

Oil seed derived biochar, OSR 550 (C 68.9±2.26 wt.%, H 1.82± 0.22 wt.%, N 1.59± 0.22 wt.%, P 0.29±0.08 wt.%, K 2.86± 0.26 wt.%, total ash 19.5±0.86 wt.%), was purchased from UK Biochar Research Centre and it was produced using a pilot-scale rotary kiln pyrolysis unit [24] setting the highest treatment temperature to 550 °C. The metal content of such powders is limited to concentration in the ppm range. Two components BFA diglycidyl resin was purchased from CORES (Cores epoxy resin, LPL).

2.2. Methods

OSR 550 biochar was annealed at temperatures of 900 °C, 1100 °C and 1500 °C by using a vacuum electric furnace (Pro.Ba., Cambiano, Italy) under argon atmosphere (99.99% purity, controlled pressure 550 mbar) using a heating rate of 150 °C/h, a dwell at the maximum temperature for 30 min and a cooling to room temperature with the same thermal gradient used for heating. Samples labelling is summarized in Table 1.

Biochar based composites were prepared according to the report of Bartoli et al. [11]. Biochars were mechanically pulverized and subsequently dispersed into the epoxy monomer using a tip ultrasonicator apparatus (Sonics Vibra-cell) for 15 min. In order to avoid an excessive temperature rise, ultrasounds were pulsed with cycles of 20 s alternating to pause of 10 s to allow a better heat diffusion. After the addition of the curing agent, the mixture was further ultrasonicated for 2 min and left into the moulds for 16 h at room temperature. A final thermal curing was performed using a ventilated oven (I.S.C.O. Srl "The scientific manufacturer") at 70 °C for 6 h. At the end, this process gives a specific surface area of the mechanically pulverized product of about 7.3 m^2/g.

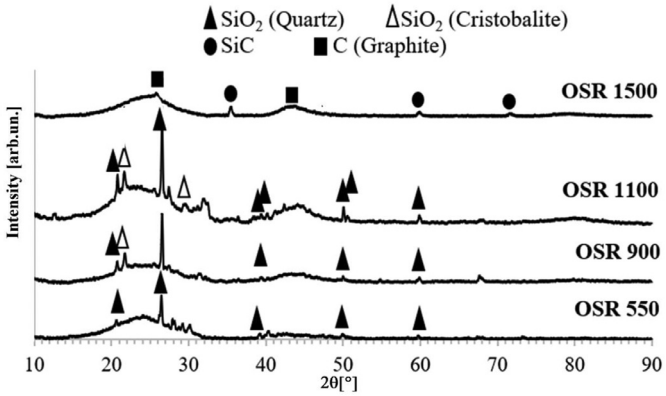

Fig. 1. XRD patterns of biochar after thermal treatment at various temperatures.

Raman spectra were collected using a Renishaw inVia (H43662 model, Gloucestershire, UK) equipped with a green laser line (514 nm) with a 50 × objective. Raman spectra were recorded in the range from 250 cm^{-1} to 3500 cm^{-1}. Decomposition of Raman spectra was focused on the range 1000–2000 cm^{-1} and performed with a homemade software developed using Matlab® (version R2020a) according to the procedure proposed by Tagliaferro et al. [25].

XPS spectra were recorded by using a PHI 5000 Versaprobe (Physical Electronics, Chanhassen, MN, USA) scanning X-ray photoelectron spectrometer (monochromatic Al K-alpha X-ray source with 1486.6 eV energy, 15 kV voltage, and 1 mA anode current) to investigate surface chemical composition.

Morphology of composites were investigated using a Field Emission Scanning Electrical microscope (FE-SEM, Zeis SupraTM 40).

XRD analyses were performed by using Panalytical X'PERT PRO PW3040/60 diffractometer, with Cu Kα radiation at 40 kV and 40 mA, Panalytical BV, Almelo, The Netherlands. The spectra were obtained from biochar powder in the 2θ range from 10 to 90° with a step size of 0.013°.

The complex permittivity of the samples was measured in the GHz range by means of a cylindrical coaxial cell (EpsiMu toolkit [26]), containing the sample as a dielectric spacer between inner and outer conductors, whose diameters are 0.6 cm and 1.3 cm, respectively. Two conical parts link the cell to standard connectors, keeping the characteristic impedance to 50 Ω, thus minimizing mismatch and energy losses. The cell is connected to a Rohde Schwarz ZVK Vector Network Analyzer, suitably calibrated, and measurements are analyzed with a two-port transmission line technique. The electromagnetic properties of the sample are determined by de-embedding and Nicolson-Ross-Weir transmission/reflection algorithm [27,28].

3. Results

3.1. Biochar characterization

OSR 550 and annealed OSR biochars were preliminary characterized by using XRD analysis and diffraction patterns are shown in Fig. 1.

Diffraction patterns of biochars showed a broad hump in the 2θ region from 16° to 32° due to the presence of a great amount of amorphous carbon, and a second broad feature between 42° and

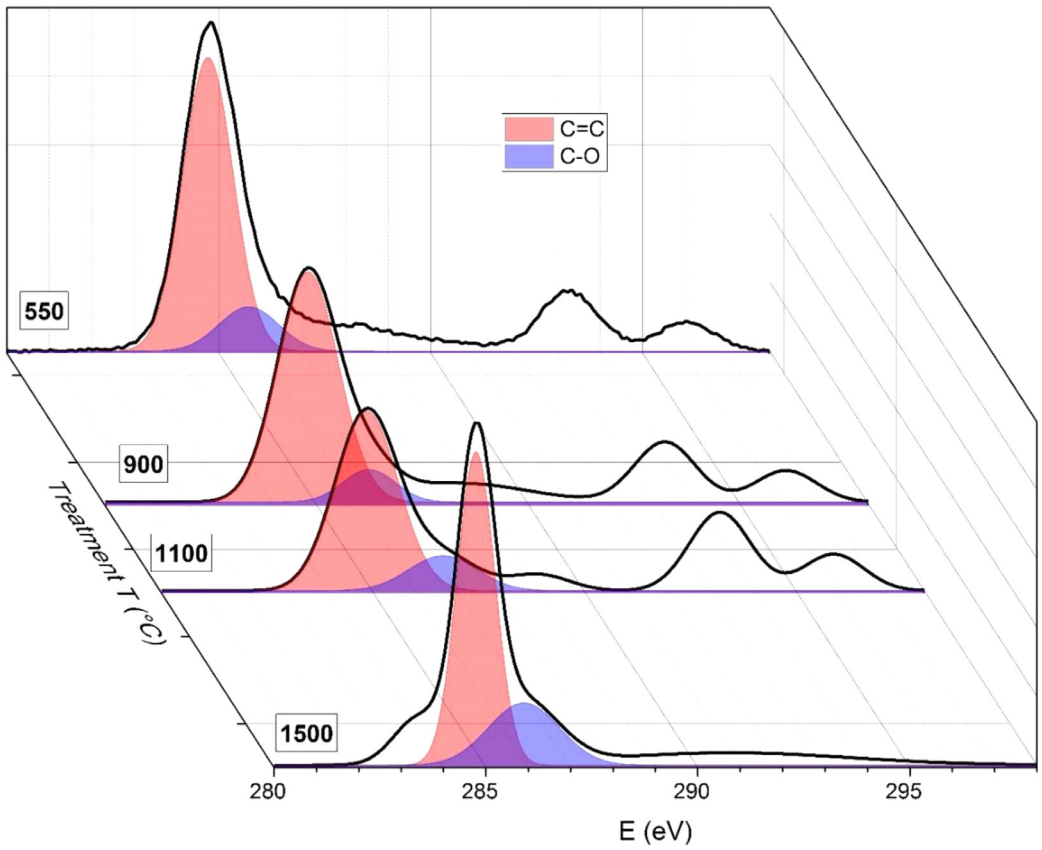

Fig. 2. XPS spectra of OSR550, OSR900, OSR1100, and OSR1500. The original XPS spectra are reported in black, the colored areas are the components of the peaks related to conducting sp^2 C atoms discussed in the text, each color identifies a specific functional group.

47° typical of sp^2 hybridized carbon. This second feature increases in intensity for higher temperature treatment of biochar, indicating a larger fraction of C atoms in this configuration and their increased connectivity [29]. OSR 1500 was the only one showing the peak at around 26°, associated to the formation of graphite (002 reflection). The band between 16° and 32° in OSR 1500 was asymmetric due to its composition comprising of two contributions centered at 20° and 25.5°, respectively [30-32]. The former is called γ-band and arises from sp^3 carbon residues linked to sp^2 crystallites edges. The latter is called Π-band and is caused by the spacing between aromatic domains layers [33]. To this second contribution belongs also the 002 reflection of graphite, resulting in a three-component complete fit of the band. More details are given in the Supplementary Material. Furthermore, OSR 1500 spectrum showed the presence of 3C-SiC phase arising from the carbothermal reaction between SiO_2 and carbon with the presence of β-SiC accordingly with Li et al. [34]. The size of the aromatic/graphitic crystallites increases with treatment temperature in the investigated samples.

OSR 550 and annealed OSR (900-1100-1500) were analyzed also by using XPS and Raman spectroscopy as summarized in Figs. 2 and 3, respectively.

XPS spectra reported in Fig. 2 were analyzed according to the components assignation proposed by Smith et al. [35]. The massive presence of sp^2 carbon (peak at 284.5 eV) was detected since the lower pyrolytic temperature investigated. This peak identifies the carbon that composes the aromatic structures. The other components reported showed the presence of C-O (peak in range from 285.2 eV up to 285.9 eV), C=O (peak at around 288 eV) and COOH (peak at around 293 eV), according to a highly tailored surface of low temperature produced materials. Interestingly, C=O and COOH are sp^2 hybridized but do not participate to graphitic conduction, representing quinoidic defects and border functionalization, respectively, as reported by Lerf–Klinowski [36]. Contrary, aromatic C-O carbon are part of the aromatic cluster due partial oxidation of boarders and actively participate to orbital delocalization and electrical conductivity. An additional peak was detected at around 296 due to $\pi-\pi^*$ satellite [37]. These components were present in all samples tested, and signal pattern changed only when an annealing temperature of 1500 °C was reached.

OSR 1500 showed a simplified spectrum without the presence of C=O related peak and with a strongly decreased COOH. C=O disappeared due the thermal decomposition and rearrangement of carbonyl functionalities [38], while carboxylic residues concentrated themselves on the borders of the graphitic domains, probably as a consequence of partial oxidation induced by air exposure [39]. Additionally, a peak at 283.4 eV was detected due to the formation of SiC as a consequence of carbothermal reduction of silica present in the original OSR [40]. As reported by Padovano et al. [41], SiC included into a carbon matrix shows continuity with carbon domains, contributing to conductivity of the material [42].

Raman spectra reported in fig. 3 enlighten the evolution of OSR 550 biochar with increasing annealing treatment temperature. The main features are the D (orange) and G (blue) peaks [43]: the former arises from aromatic rings confined in defective graphitic structures and is related to the size of crystallites [44] and their edges [45], while the latter is related to in-plane carbon sp^2 bonds stretching.

As discussed in detail by Tagliaferro et al. [25], in all spectra, D and G peaks were fitted by two components each (G^1, G^2, D^1, D^2) with the exception of OSR 550 where the presence of $CaCO_3 \cdot nH_2O$ [46] required an additional component centered at 1700 cm^{-1}. This

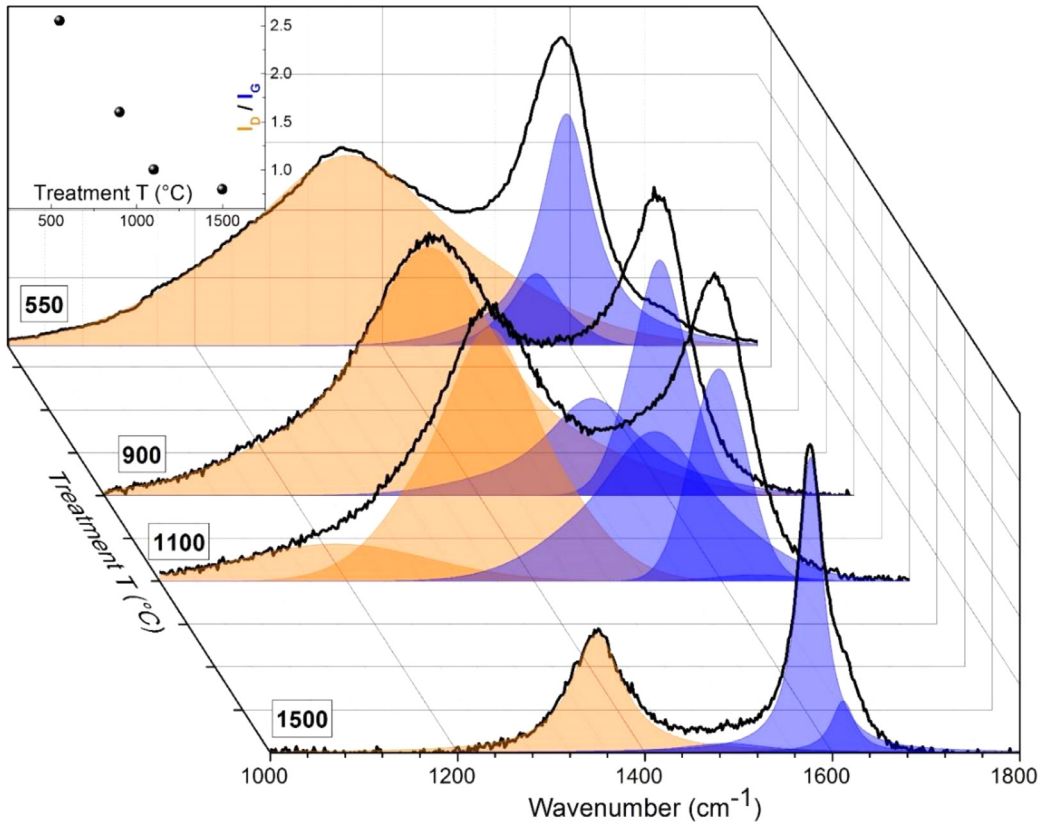

Fig. 3. Raman spectra of OSR550, OSR900, OSR1100, and OSR1500. The original Raman spectra are reported in black; the colored areas are the components of the D (orange) and G (blue) peaks, discussed in the text. The inset shows the increase of the I_D/I_G ratio with treatment temperature, indicating the transition towards the formation of graphitic crystallites.

component disappeared due to the decomposition of carbonates at temperature beyond 900 °C [47]. According to ref. [25], the G^1 peak intensity is proportional to the reduction of interlayers spacing of aromatic layers and the increment of graphitic crystallites, while G^2 is related with bond angle disorder as suggested by Shimodaira et al. [48]. G^1 and G^2 peak positions were centered respectively between 1546–1580 cm^{-1} and 1590–1612 cm^{-1} (drifts are due to the thermal treatment [49]). The interpretation of the D components (centered between 1159–1480 and 1369–1377, for D^1 and D^2 respectively) was more complex, and we hypothesized that they rose from two different but similar phenomena. According to Shimodaira et al. [48], D components were both related to angle disorder related to graphitic domains misalignment induced by inorganic components uniformly dispersed in the carbon matrix. During the sp^2 carbon clusters growth, inorganics were excluded from the growing area inducing at the same time a stress on the aromatic domains. As an example, SiC region embedded into aromatic domains of OSR 1500 can perturb the bond angles of carbon planes originating the band D^1.

The ratio of the intensities of the two peaks (I_D/I_G), shown in the inset of fig. 3, is the most relevant feature that can be extracted for the following discussion, as it is a measure of the evolution from amorphous carbon to nanocrystalline graphite. This ratio decreases with higher treatment temperature, indicating an increasing contribution from graphitic domains, also in agreement with the XRD data discussed above.

OSRs were then mixed with epoxy resin and composites were analysed through FESEM, after cryofracture, as reported in fig. 4.

The analysis showed that OSR 1500 particles, with diameter ranging from 20 μm to 200 μm, were quite uniformly dispersed and well embedded into the epoxy matrix. Particles were not infiltrated by epoxy matrix, and their close surrounding environment was deformed by the carbon particles presence, showing the discoidal artefacts shown in Fig. 4. These formations were reasonably due to the high biochar loading that induce a high stress in the crystalline structure of the resin. As previously reported by Das et al. [50], the infiltration of filler in the biochar porosity is strictly related to the pore average size: in the present case, the pores, ranging from 1 μm to 5 μm, prevent the infiltration phenomenon.

3.2. Composites characterization

The electromagnetic properties of the composite and its components in the GHz frequency range were then analyzed through the evaluation of their complex relative permittivity, that can be defined as:

$$\varepsilon = \varepsilon' - j\varepsilon'' = \varepsilon' - j\left(\frac{\sigma}{\omega\varepsilon_0} + \varepsilon''_d\right) \quad (1)$$

where $j = \sqrt{-1}$, σ is the conductivity, ω is the angular frequency, and ε_0 is the permittivity of the vacuum. The real part of the dielectric constant, ε', is mainly associated with the polarizability of the medium, and the imaginary part ε'' to losses, with ε_d'' representing relaxation, i.e. the dissipation energy during polarization and depolarization process. Usually, in the microwave domain the σ term is dominant [51]. Moreover, the electric loss tangent, $\tan\delta_\varepsilon$, and the microwave penetration depth, d_p, can be calculated starting from the complex permittivity, as $\tan\delta_\varepsilon = \varepsilon''/\varepsilon'$ and $d_p = \frac{\sqrt{2}c}{\omega}[\varepsilon'(\sqrt{1+(\tan\delta_\varepsilon)^2}-1)]^{-1/2}$, respectively.

Fig. 5 shows the real part of the complex permittivity and the conductivity, as a function of frequency.

To highlight the behaviors as a function of the biochar weight fraction and of the treatment temperature, we report in Fig. 6 both

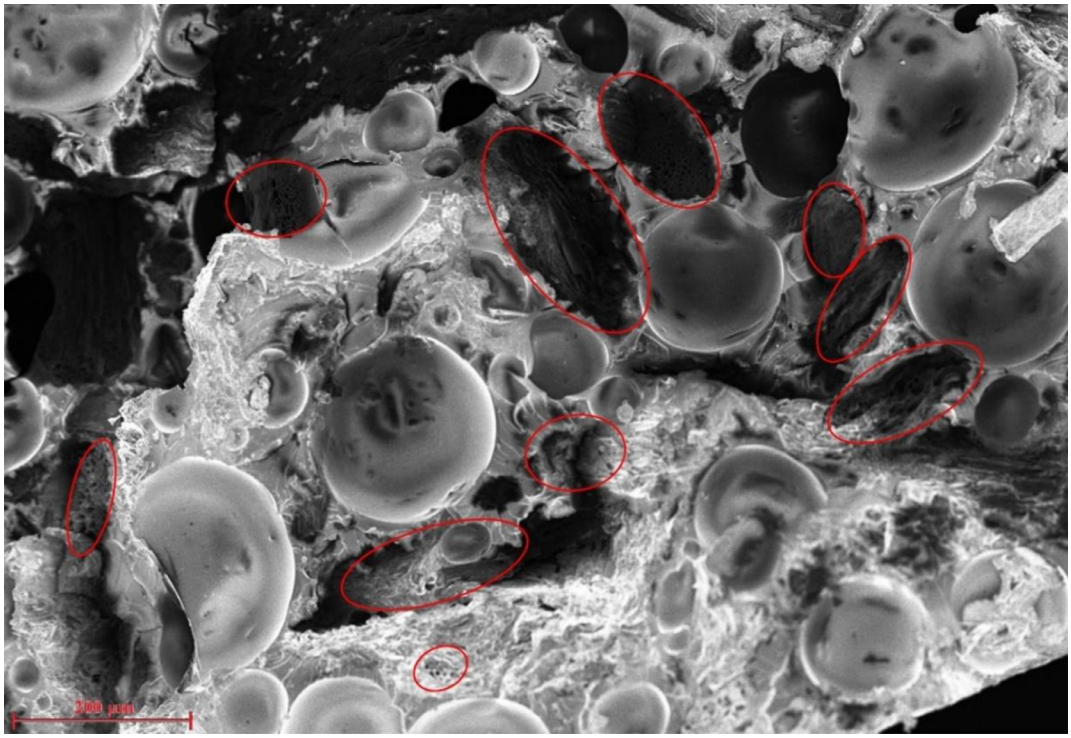

Fig. 4. FESEM image of composites containing 25 wt.% of OSR 1500. Biochar particles are circled in red.

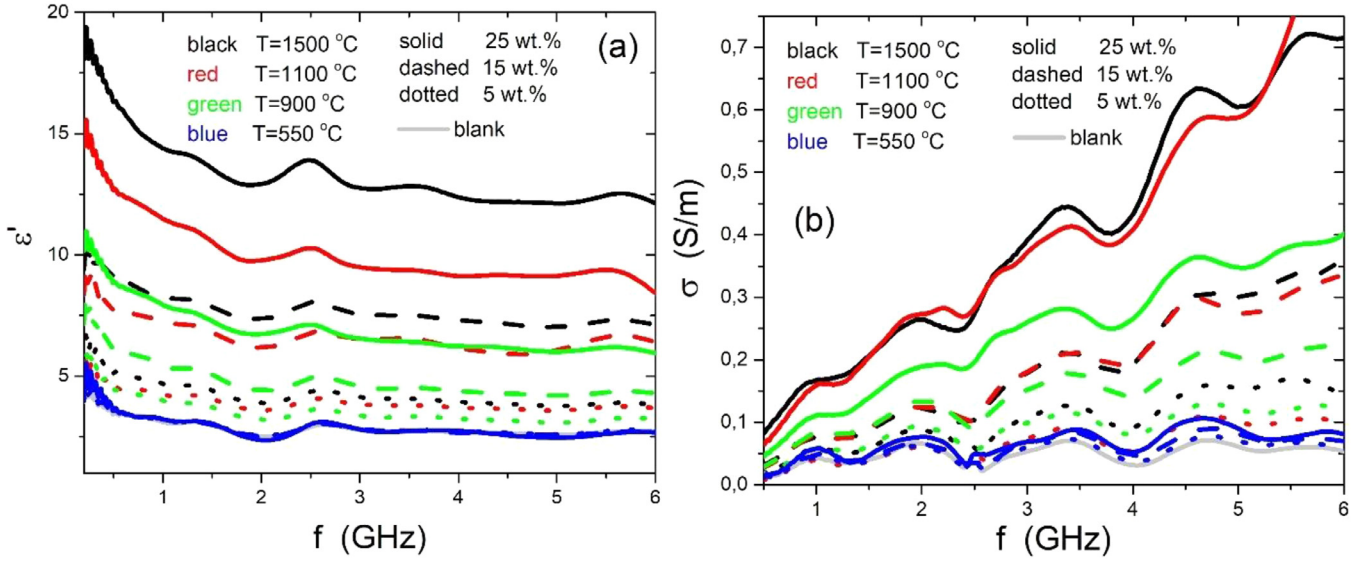

Fig. 5. Real part of the complex permittivity (a) and conductivity (b) as a function of frequency, measured for the composites prepared at different temperatures and with different weight fraction of biochar, as reported in the legend.

the real part of the permittivity and the conductivity at the reference frequency of 5 GHz. Composites prepared using OSR 550 showed values not significantly different from the blank sample, while increasing values are shown at increasing temperature and weight fraction.

In order to extract the information concerning the electromagnetic properties of the biochar inclusions from the overall response of the composite, one needs to express the effective permittivity of the composite as a function of permittivity of each constituent and volume concentration of the filler, the so-called mixing rule. Several approaches have been reported in literature [52–54], and for many of them, the general formula of the effective permittivity ε_{eff} for a two-phase system, as the one we are investigating, can be defined according to the following equation [55,56]

$$\varepsilon_{eff}{}^{\alpha} = (1-f)\varepsilon_m{}^{\alpha} + f\varepsilon_b{}^{\alpha} \quad (2)$$

where the exponent is in the range $-1 \le \alpha \le 1$, ε_m is the complex permittivity of the epoxy matrix, ε_b is the complex permittivity of the biochar inclusions, and f is the volume fraction of the inclusions with respect to the total sample volume. We adopted the Looyenga's approach [54], which does not involve any assumption about the shape of the inclusions: for any particle geometry, the mixing formula is Eq. (2) with $\alpha = 1/3$. Fig. 7 shows the results for our samples, with the ε_b' and σ_b curves corresponding to the com-

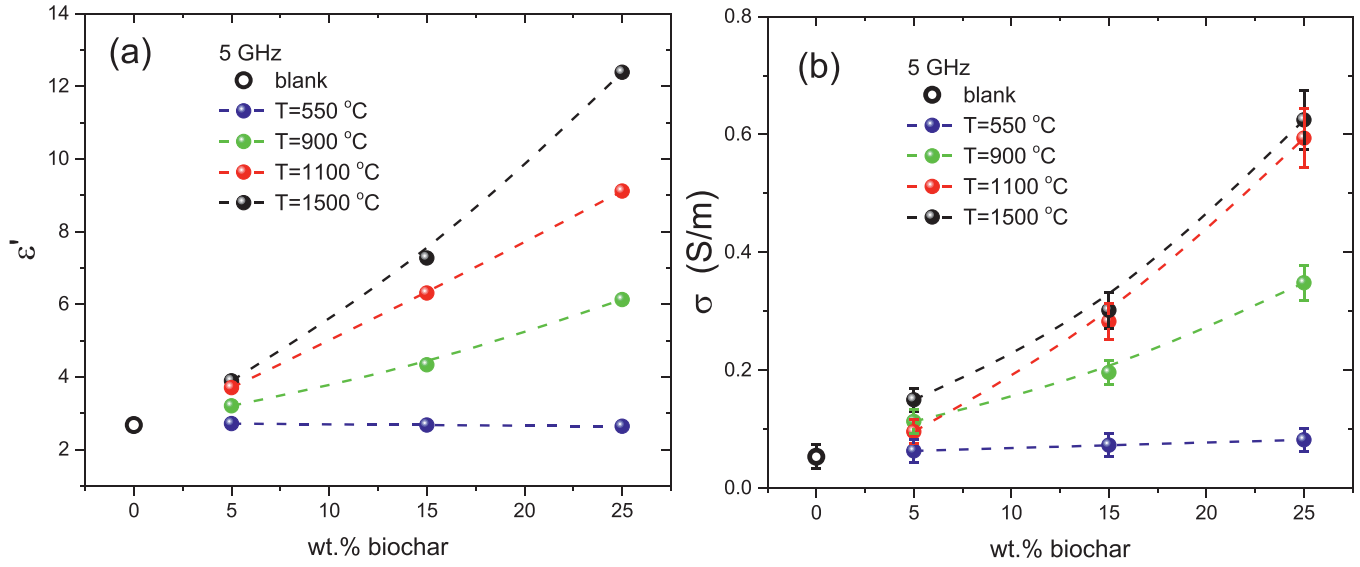

Fig. 6. Real part of the complex permittivity (a) and conductivity (b) at the frequency of 5 GHz, as a function of the biochar weight fraction. Dashed lines are guides to the eye.

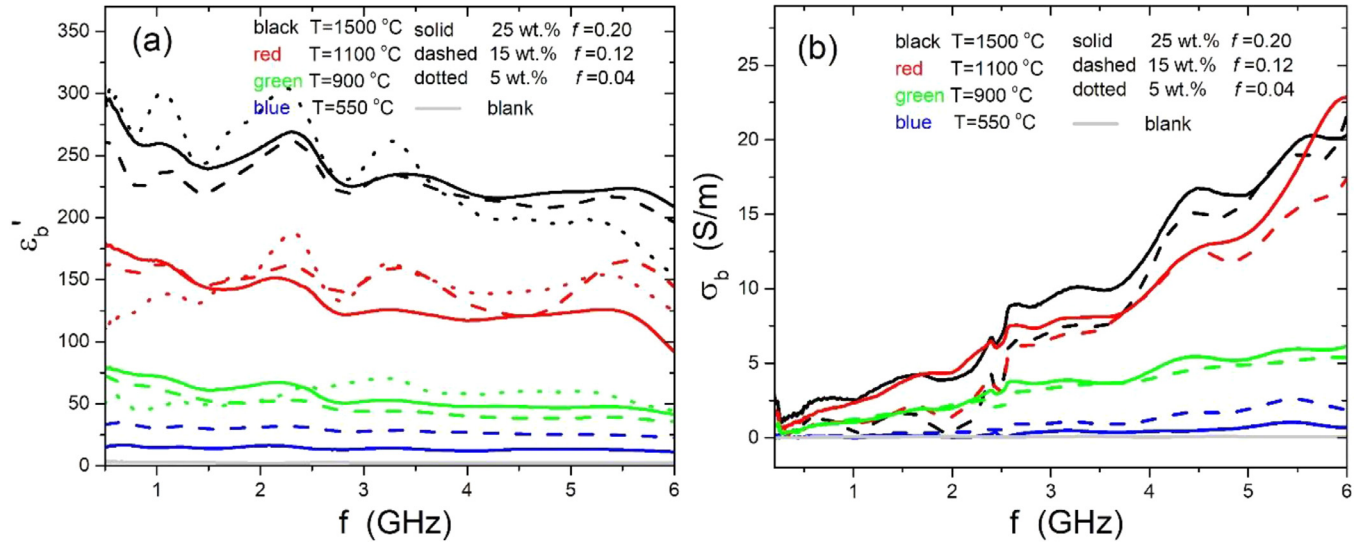

Fig. 7. Real part of the complex permittivity (a) and conductivity (b) of the biochar inclusions, obtained with the deconvolution method described in the text.

positions prepared at the same temperature represented by curves with the same color. The volume fraction f was estimated by direct FESEM observation (see Fig. 4) on 25 wt.% samples according to the approach proposed by Dong et al. [57] and it was evaluated to be f=0.20, with a percentage error of the order of 10%, evaluated by the analysis of several 500 μm × 500 μm images taken from different areas of cryo-fractured samples. Accordingly, for the other samples with 15 wt.% and 5 wt.% biochar inclusions, f was assumed to be 0.12 and 0.04, i.e. proportional to the weight fraction. This assumption is justified by the uniformity of dispersions achieved after the sonication process, as reported in Ref. [11], and by the microwave analysis itself, since the ε_b' and σ_b curves for biochar inclusions prepared with the same treatment temperature nicely scale, collapsing on the same trend when f=0.2, 0.12, and 0.04 is assumed (Fig. 7).

The deconvolution method is validated by the observation that the curves corresponding to the three compositions prepared at the same temperature almost collapse to a single behavior (within the amplitude of the spurious experimental ripples due to the non-ideality of the measurement). The sample with the smallest volume fraction prepared at the lowest temperature is not always reported, since it is too close to the curve of the blank sample to allow a meaningful extraction of the biochar characteristics. A difference still persists between the curves of samples treated at different temperatures, reflecting the variation of the electromagnetic properties of different biochar inclusions.

In Fig. 8, we report the behavior of ε' and σ as a function of treatment temperature, for both the composite and the biochar inclusion alone, at the reference frequency of 5 GHz.

Data show a remarkable enhancement of real permittivity and conductivity with the increment of temperature even if OSR based materials are non-graphitizable carbons [58]. As a reference, we note that the values of complex permittivity after the 1500° heat treatment correspond to a loss tangent and a penetration depth of $\tan\delta_\varepsilon$ = 0.178 (0.267) and d_p = 31 mm (4.8 mm) for the composite (biochar inclusions), respectively.

Microwave conductivity of OSR 550, OSR 900, OSR 1100 are comparable with those measured for the coffee treated at 600 °C, 800 °C and 1000 °C respectively [17]. OSR 1500 showed a higher biochar conductivity of up to 17 S/m, according to the higher de-

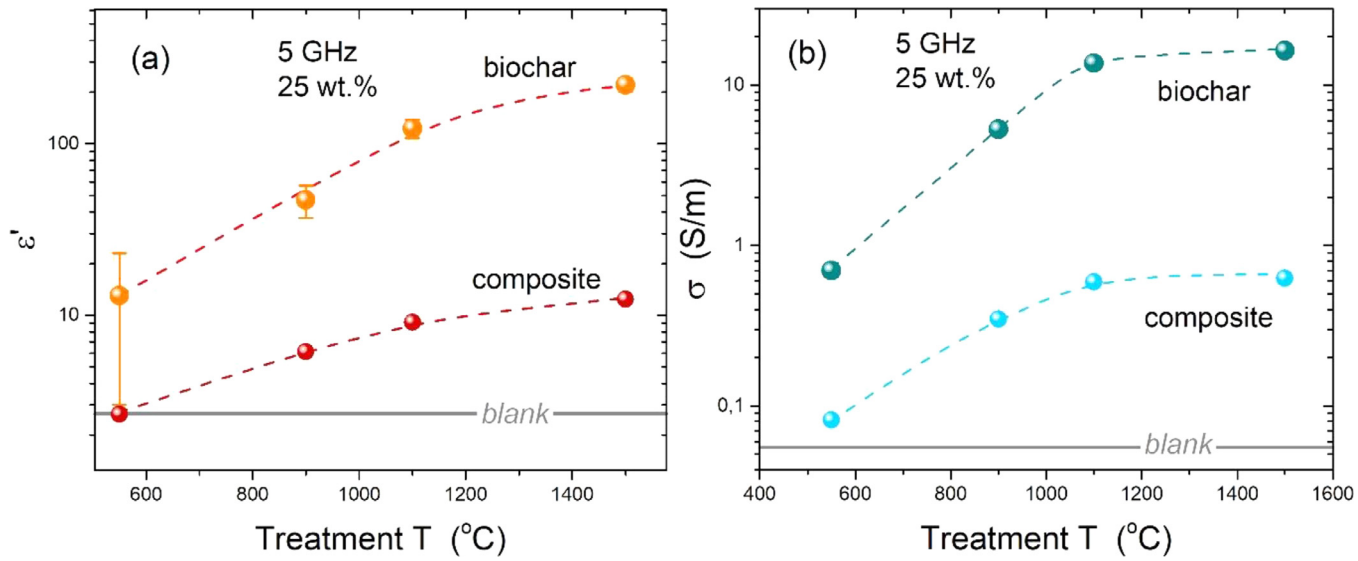

Fig. 8. Dependence of the real part of the complex permittivity (a) and conductivity (b) from the preparation temperature, at the frequency of 5 GHz. Data are extracted from the 25 wt.% curves, which show the largest difference from the neat. (Note the log scale on the vertical axis).

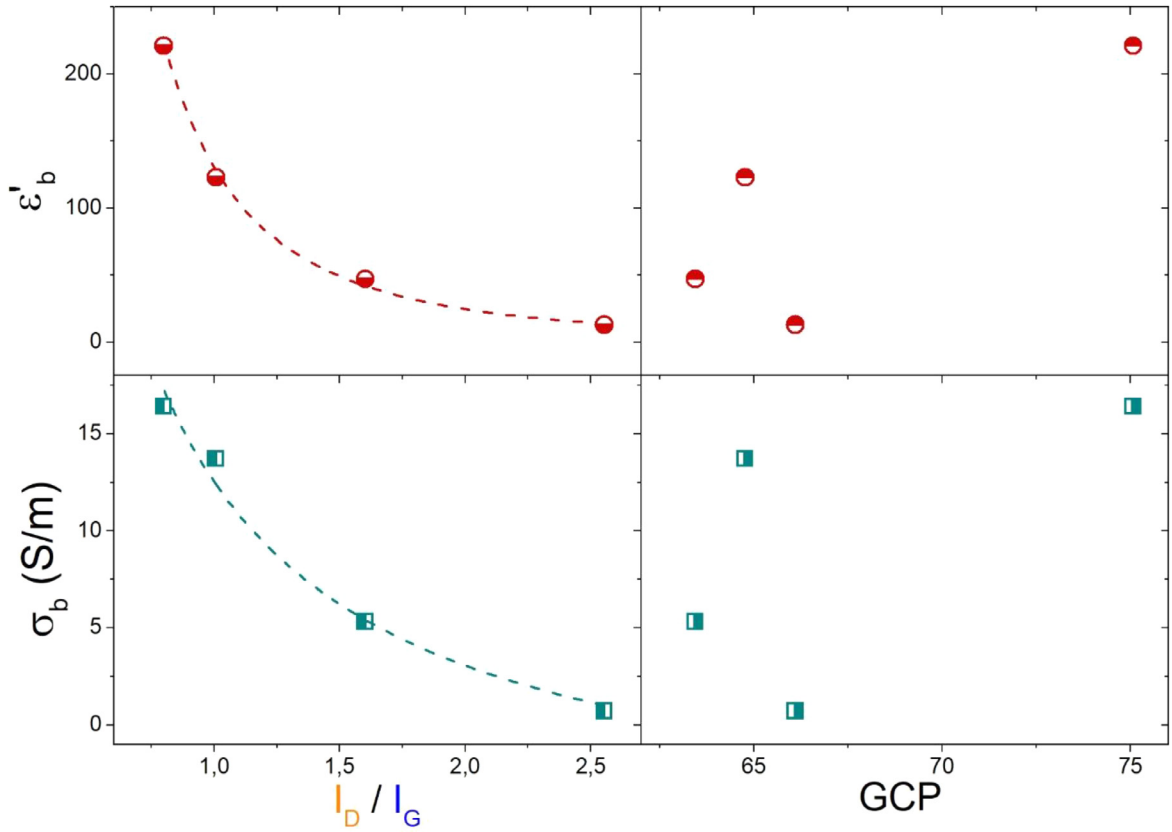

Fig. 9. Dependence of the real part of the complex permittivity (top panels) and conductivity (bottom panels) of biochar, at the frequency of 5 GHz, from the I_D/I_G ratio of Raman peaks (left panels) and from the graphitic carbon percentage (GCP) deduced from XPS spectra. Data are extracted from the 25 wt.% curves, which show the largest difference from the blank. The I_D/I_G ratio increases with the transition from amorphous carbon to nanocrystalline graphite.

gree of graphitization observed by both XRD and Raman analysis. Nonetheless, composites containing 25 wt.% of OSR 1100 and OSR 1500 showed similar values of conductivity, suggesting that percolation threshold of OSR 1500 was not yet reached.

It is interesting to compare the behavior of the biochar inclusions as a function of treatment temperature (Fig. 7) with that of the biochar inclusions as a function of the I_D/I_G ratio and graphitic carbon percentage (GCP) calculated as the percentage of XPS signal from C=C and C-O identified in Fig. 9. This allows to gain a better insight into the structural details and opens to the optimization of the radiofrequency properties. In fact, the I_D/I_G ratio is a measure of the transformation from amorphous carbon to nanocrystalline graphite (increasing order for decreasing values), whilst the GCP directly characterizes the local properties of the biochar. When the electromagnetic properties are plotted directly against the I_D/I_G ratio, no saturation is found and data clearly show a correlation

(Fig. 9, left panels). Conversely, when data are plotted against the GCP, no clear correlation emerges (Fig. 9, right panels). The lack of correlation between GCP and conductivity should be interpreted in light of the characteristics of the technique used: XPS analysis mainly scans the investigated material surface [59], representative in this case of the interface with the polymeric matrix, while Raman spectroscopy could reach a depth inside a carbon sample up to about 1 μm, by using a wavelength of 532 nm [60]. Therefore, the observed trends enlighten a strong correlation between long range order detected through Raman spectroscopy while interphase properties investigated through XPS seem not to significantly affect the conductivity evolution. Moreover, since the composition of this kind of biochar is quite uniform, this absence of correlation with GCP suggests that it is more convenient to work on the ordering of biochar particles rather than on the percentage of sp^2 C when optimizing these materials for high frequency applications. OSR series displayed a very high amount of aromatic carbons already from the bottom of the temperature range explored in the present study, but showed a relevant electrical conductivity only after further thermal treatments. This proved that isolated aromatic clusters are not sufficient for promoting conductivity since they need to form proper graphitic domains. In the OSR series showed this reorganization between OSR 550 and OSR 900, while OSR 1100 and OSR 1500 are characterized by the enlargement of graphitic domains. The difference between formation and enlargement lays behind the different conductivity values observed.

4. Conclusions

In this work, we correlated the structural changes induced by thermal annealing of OSR with the complex permittivity and conductivity properties measured in OSR-epoxy composites in the GHz frequency range. Data collected clearly showed an increment of both the real part of permittivity and of conductivity with increasing treatment temperature. This can be correlated with the ordering process induced by annealing that leads to a higher degree of graphitization in OSR, as observed by both Raman and XRD analysis. The highest biochar conductivity is estimated in 17 S/m, while ε' reached 220 for an annealing temperature of 1500 °C.

The biochar conductivity trends with treatment temperature were preserved in the related epoxy-based composites, although with reduced differences between OSR 1100 and OSR 1500. Increasing biochar concentration in the epoxy matrix increases both ε' and σ in a slightly supralinear fashion, allowing easy tuning of the composite properties.

We clearly reported the dependence of electromagnetic properties of biochar to the order of the carbon structures while the carbonization degree expressed as the percentage of carbon insert into aromatic systems able to participate to orbital delocalization seems not to influence the observed properties.

Overall, this work indicates a path for the engineering of the electromagnetic properties of biochar composites in the microwave frequency range.

Declaration of Competing Interest

The authors declare that they have no known competing financial interests or personal relationships that could have appeared to influence the work reported in this paper.

Acknowledgments

Authors wish to thank to Elisa Padovano for biochar thermal treatments and XRD spectra and Salvatore Guastella for FESEM and XPS analysis.

Supplementary materials

Supplementary material associated with this article can be found, in the online version, at doi:10.1016/j.cartre.2021.100062.

References

[1] V. Veleva, M. Ellenbecker, Indicators of sustainable production: framework and methodology, J. Clean. Prod. 9 (6) (2001) 519–549.
[2] O. Ioannidou, A. Zabaniotou, Agricultural residues as precursors for activated carbon production—a review, Renew. Sustain. Energy Rev. 11 (9) (2007) 1966–2005.
[3] S. Awasthi, J.L. Wood, Carbon/carbon composite materials for aircraft brakes, in: Proceedings of the 12th Annual Conference on Composites and Advanced Ceramic Materials: Ceramic Engineering and Science Proceedings, Wiley Online Library, 1988, pp. 553–559.
[4] Q. Truong, Composite architecture: the technology and design of carbon fiber and FRPs, Compos. Archit. (2020) Birkhäuser.
[5] M. Vochozka, A. Maroušková, J. Váchal, J. Straková, Biochar pricing hampers biochar farming, Clean Technol. Environ. Policy 18 (4) (2016) 1225–1231.
[6] L. Xiao, L. Feng, G. Yuan, J. Wei, Low-cost field production of biochars and their properties, Environ. Geochem. Health 42 (6) (2020) 1569–1578.
[7] M. Bartoli, M. Giorcelli, P. Jagdale, M. Rovere, A. Tagliaferro, A review of non–soil biochar applications, Materials 13 (2) (2020) 291–296.
[8] S.P. Sohi, E. Krull, E. Lopez-Capel, R. Bol, A review of biochar and its use and function in soil, in: Advances in agronomy, Elsevier, 2010, pp. 47–82.
[9] A. Khan, P. Savi, S. Quaranta, M. Rovere, M. Giorcelli, A. Tagliaferro, C. Rosso, C.Q. Jia, Low-cost carbon fillers to improve mechanical properties and conductivity of epoxy composites, Polymers 9 (12) (2017) 642.
[10] A. Khan, P. Jagdale, M. Rovere, M. Nogués, C. Rosso, A. Tagliaferro, Carbon from waste source: an eco-friendly way for strengthening polymer composites, Compos. Part B: Eng. 132 (2018) 87–96.
[11] M. Bartoli, M. Giorcelli, C. Rosso, M. Rovere, P. Jagdale, A. Tagliaferro, Influence of commercial biochar fillers on brittleness/ductility of epoxy resin composites, Appl. Sci. 9 (15) (2019) 13.
[12] M. Bartoli, M.A. Nasir, E. Passaglia, R. Spiniello, P. Jagdale, C. Rosso, M. Giorcelli, M. Rovere, A. Tagliaferro, Influence of pyrolytic thermal history on olive pruning biochar and related epoxy composites mechanical properties, J. Compos. Mater. 54 (14) (2020) 1863–1873.
[13] M. Bartoli, C. Rosso, M. Giorcelli, M. Rovere, P. Jagdale, A. Tagliaferro, M. Chae, D.C. Bressler, Effect of incorporation of microstructured carbonized cellulose on surface and mechanical properties of epoxy composites, J. Appl. Polym. Sci. 137 (27) (2020) 48896.
[14] S. Li, S. Harris, A. Anandhi, G. Chen, Predicting biochar properties and functions based on feedstock and pyrolysis temperature: a review and data syntheses, J. Clean. Prod. 215 (2019) 890–902.
[15] A. Tomczyk, Z. Sokołowska, P. Boguta, Biochar physicochemical properties: pyrolysis temperature and feedstock kind effects, Rev. Environ. Sci. Bio/Technol. 19 (2020) 191–215.
[16] A. Noori, M. Bartoli, A. Frache, E. Piatti, M. Giorcelli, A. Tagliaferro, Development of pressure-responsive polypropylene and biochar-based materials, Micromachines 11 (4) (2020) 339.
[17] M. Giorcelli, M. Bartoli, Development of coffee biochar filler for the production of electrical conductive reinforced plastic, Polymers 11 (12) (2019) 17.
[18] M. Bartoli, M. Giorcelli, M. Rovere, P. Jagdale, A. Tagliaferro, M. Chae, D.C. Bressler, Shape tunability of carbonized cellulose nanocrystals, SN Appl. Sci. 1 (12) (2019) 1661–1676.
[19] M. Giorcelli, P. Savi, A. Khan, A. Tagliaferro, Analysis of biochar with different pyrolysis temperatures used as filler in epoxy resin composites, Biomass Bioenergy 122 (2019) 466–471.
[20] M. Giorcelli, A. Khan, N.M. Pugno, C. Rosso, A. Tagliaferro, Biochar as a cheap and environmental friendly filler able to improve polymer mechanical properties, Biomass Bioenergy 120 (2019) 219–223.
[21] P. Savi, M. Yasir, M. Bartoli, M. Giorcelli, M. Longo, Electrical and microwave characterization of thermal annealed sewage sludge derived biochar composites, Applied Sciences 10 (4) (2020) 1334–1345.
[22] A. Downie, A. Crosky, P. Munroe, Physical Propierties of Biochar, Biochar for Environmental Management: Science and Technology, J. Lehmann, S. Joseph (Eds.), Earthscan Ltd., London, 2009.
[23] Y. Eom, S.M. Son, Y.E. Kim, J.-E. Lee, S.-H. Hwang, H.G. Chae, Structure evolution mechanism of highly ordered graphite during carbonization of cellulose nanocrystals, Carbon 150 (2019) 142–152.
[24] O. Mašek, W. Buss, A. Roy-Poirier, W. Lowe, C. Peters, P. Brownsort, D. Mignard, C. Pritchard, S. Sohi, Consistency of biochar properties over time and production scales: A characterisation of standard materials, J. Anal. Appl. Pyrolysis 132 (2018) 200–210.
[25] A. Tagliaferro, M. Rovere, E. Padovano, M. Bartoli, M. Giorcelli, Introducing the novel mixed Gaussian-Lorentzian lineshape in the analysis of the Raman signal of biochar, Nanomaterials 10 (9) (2020) 1748.
[26] D. Ba, P. Sabouroux, Epsimu, a toolkit for permittivity and permeability measurement in microwave domain at real time of all materials: applications to solid and semisolid materials, Microw. Opt. Technol. Lett. 52 (12) (2010) 2643–2648.
[27] A. Nicolson, G. Ross, Measurement of the intrinsic properties of materials by time-domain techniques, IEEE Trans. Instrum. Meas. 19 (4) (1970) 377–382.

[28] J. Baker-Jarvis, E.J. Vanzura, W.A. Kissick, Improved technique for determining complex permittivity with the transmission/reflection method, IEEE Trans. Microw. Theory Tech. 38 (8) (1990) 1096–1103.
[29] M. Kawakami, H. Kanba, K. Sato, T. Takenaka, S. Gupta, R. Chandratilleke, V. Sahajwalla, Characterization of thermal annealing effects on the evolution of coke carbon structure using Raman spectroscopy and X-ray diffraction, ISIJ Int. 46 (8) (2006) 1165–1170.
[30] B. Manoj, Investigation of nanocrystalline structure in selected carbonaceous materials, Int. J. Miner. Metall. Mater. 21 (9) (2014) 940–946.
[31] H. Takagi, K. Maruyama, N. Yoshizawa, Y. Yamada, Y. Sato, XRD analysis of carbon stacking structure in coal during heat treatment, Fuel 83 (17-18) (2004) 2427–2433.
[32] Z. Li, C. Lu, Z. Xia, Y. Zhou, Z. Luo, X-ray diffraction patterns of graphite and turbostratic carbon, Carbon 45 (8) (2007) 1686–1695.
[33] B. Manoj, A. Kunjomana, Study of stacking structure of amorphous carbon by X-ray diffraction technique, Int. J. Electrochem. Sci 7 (4) (2012) 3127–3134.
[34] X. Li, X. Chen, H. Song, Synthesis of β-SiC nanostructures via the carbothermal reduction of resorcinol–formaldehyde/SiO_2 hybrid aerogels, J. Mater. Sci. 44 (17) (2009) 4661–4667.
[35] M. Smith, L. Scudiero, J. Espinal, J.-S. McEwen, M. Garcia-Perez, Improving the deconvolution and interpretation of XPS spectra from chars by ab initio calculations, Carbon 110 (2016) 155–171.
[36] A. Lerf, H. He, T. Riedl, M. Forster, J. Klinowski, 13C and 1H MAS NMR studies of graphite oxide and its chemically modified derivatives, Solid State Ion. 101 (1997) 857–862.
[37] P.S. Bagus, E.S. Ilton, C.J. Nelin, The interpretation of XPS spectra: insights into materials properties, Surf. Sci. Rep. 68 (2) (2013) 273–304.
[38] I. Sengupta, S.S.S. Kumar, S.K. Pal, S. Chakraborty, Characterization of structural transformation of graphene oxide to reduced graphene oxide during thermal annealing, J. Mater. Res. 35 (9) (2020) 1197–1204.
[39] D.L. Perry, A. Grint, Application of XPS to coal characterization, Fuel 62 (9) (1983) 1024–1033.
[40] W.S. Seo, K. Koumoto, Stacking faults in β-SiC formed during carbothermal reduction of SiO_2, J. Am. Ceram. Soc. 79 (7) (1996) 1777–1782.
[41] E. Padovano, M. Giorcelli, G. Bianchi, S. Biamino, M. Rovere, A. Tagliaferro, A. Ortona, Graphite-Si-SiC ceramics produced by microwave assisted reactive melt infiltration, J. Eur. Ceram. Soc. 39 (7) (2019) 2232–2243.
[42] Q. Li, Y. Zhang, H. Gong, H. Sun, T. Li, X. Guo, S. Ai, Effects of graphene on the thermal conductivity of pressureless-sintered SiC ceramics, Ceram. Int. 41 (10) (2015) 13547–13552.
[43] D.B. Schuepfer, F. Badaczewski, J.M. Guerra-Castro, D.M. Hofmann, C. Heiliger, B. Smarsly, P.J. Klar, Assessing the structural properties of graphitic and non–graphitic carbons by Raman spectroscopy, Carbon 161 (2020) 359–372.
[44] F. Tuinstra, J.L. Koenig, Raman spectrum of graphite, J. Chem. Phys. 53 (3) (1970) 1126–1130.
[45] F. Negri, E. di Donato, M. Tommasini, C. Castiglioni, G. Zerbi, K. Müllen, Resonance Raman contribution to the D band of carbon materials: modeling defects with quantum chemistry, J. Chem. Phys. 120 (24) (2004) 11889–11900.
[46] M. Tlili, M.B. Amor, C. Gabrielli, S. Joiret, G. Maurin, P. Rousseau, Characterization of $CaCO_3$ hydrates by micro-Raman spectroscopy, J. Raman Spectrosc. 33 (1) (2002) 10–16.
[47] K. Tonsuaadu, K.A. Gross, L. Plūduma, M. Veiderma, A review on the thermal stability of calcium apatites, J. Therm. Anal. Calorim. 110 (2) (2012) 647–659.
[48] N. Shimodaira, A. Masui, Raman spectroscopic investigations of activated carbon materials, J. Appl. Phys. 92 (2) (2002) 902–909.
[49] A.C. Ferrari, J. Robertson, Interpretation of Raman spectra of disordered and amorphous carbon, Phys. Rev. B 61 (20) (2000) 14095.
[50] O. Das, A.K. Sarmah, D. Bhattacharyya, Structure–mechanics property relationship of waste derived biochars, Sci. Total Environ. 538 (2015) 611–620.
[51] A. Kumar, S. Sharma, G. Singh, Measurement of dielectric constant and loss factor of the dielectric material at microwave frequencies, (2007).
[52] J.M. Garnett XII, Colours in metal glasses and in metallic films, Philos. Trans. R. Soc. Lond. Ser. A, Contain. Pap. Math. Phys. Char. 203 (359-371) (1904) 385–420.
[53] V.D. Bruggeman, Berechnung verschiedener physikalischer Konstanten von heterogenen Substanzen. I. Dielektrizitätskonstanten und Leitfähigkeiten der Mischkörper aus isotropen Substanzen, Ann. Phys. Lpz. 416 (7) (1935) 636–664.
[54] H. Looyenga, Dielectric constants of heterogeneous mixtures, Physica 31 (3) (1965) 401–406.
[55] T. Zakri, J.-P. Laurent, M. Vauclin, Theoretical evidence forLichtenecker's mixture formulae'based on the effective medium theory, J. Phys. D Appl. Phys. 31 (13) (1998) 1589.
[56] A. Brovelli, G. Cassiani, Effective permittivity of porous media: a critical analysis of the complex refractive index model, Geophys. Prospect. 56 (5) (2008) 715–727.
[57] M. Dong, S. Schmauder, Modeling of metal matrix composites by a self-consistent embedded cell model, Acta Mater. 44 (6) (1996) 2465–2478.
[58] R.E. Franklin, Crystallite growth in graphitizing and non-graphitizing carbons, Proc. Royal Soc. Lond. Ser. A. Math. Phys. Sci. 209 (1097) (1951) 196–218.
[59] B. Lesiak, L. Kövér, J. Tóth, J. Zemek, P. Jiricek, A. Kromka, N. Rangam, C sp_2/sp_3 hybridisations in carbon nanomaterials – XPS and (X)AES study, Appl. Surf. Sci. 452 (2018) 223–231.
[60] N.J. Everall, Modeling and measuring the effect of refraction on the depth resolution of confocal Raman microscopy, Appl. Spectrosc. 54 (6) (2000) 773–782.